 doi:10.20944/preprints202209.0075.v1

Article

Influence of a Flat Polyimide Inlay on the Propagation of Guided Ultrasonic Waves in a Narrow GFRP-Specimen

Liv Rittmeier [1]*, Thomas Roloff [1], Natalie Rauter[2], Andrey Mikhaylenko[2], Jan Niklas Haus[3], Rolf Lammering[2], Andreas Dietzel[3] and Michael Sinapius [1]

[1] Institute of Mechanics and Adaptronics, Technische Universität Braunschweig, 38106 Braunschweig, Germany
[2] Chair of Mechanics, Helmut-Schmidt-University / University of the Federal Armed Forces Hamburg, 22043 Hamburg, Germany
[3] Institute of Microtechnology, Technische Universität Braunschweig, 38124 Braunschweig, Germany
* Correspondence: l.rittmeier@tu-braunschweig.de; Tel.: +49-531-391-2682

Abstract: This work investigates how integrated polyimide inlays with applied sensor bodies influence the guided ultrasonic wave propagation in narrow glass fiber-reinforced polymer specimens. Preliminary numerical simulations indicate that in a damping-free specimen, the inlays show reflections for the S_0-mode propagation. Hence, an air-coupled ultrasonic technique and a 3D laser Doppler vibrometer measurement are used to measure different parts of the propagating waves' displacement field after burst excitation at different frequencies. No significant reflections on the inlay can be seen in the experiments. However, it is shown that the reflections from the strip specimen's narrow width cause periodical reflections that superimpose with the excited wave fronts. A continuous wavelet transformation in the time-frequency domain filters discontinuities from the measurement signal and is used for reconstruction of the time signals. The reconstructed signals are used in a spatial continuous wavelet transformation to identify the occurring wavelengths and hence to prove the assumption of reflections from the narrow edges. Since the amplitude of the reflections identified in the numerical data at the polyimide inlays are an order of magnitude smaller than the excited wave packages, it is concluded that material damping of the epoxy resin matrix extincts possible reflections from the inlays.

Keywords: structural health monitoring; narrow specimen; guided ultrasonic waves; continuous wavelet transformation; numerical simulation; composite materials; GFRP

1. Introduction

Structural health monitoring (SHM) using guided ultrasonic waves (GUW) has been of great interest in research for the detection of structural damage [1–4]. GUW can travel over long distances in thin-walled structures without dissipating much energy and interact with changes in acoustic impedance caused by inhomogeneities such as damage [4]. These interactions result in reflections, scattering, mode conversions and amplitude attenuation, which can be observed in the wave field [5,6]. Therefore, changes in the wave propagation are an indicator for damage, which can be detected using different measurement techniques such as laser vibrometry [7], air-coupled technique [8] or piezoelectric sensors [1]. Laser vibrometry and an air-coupled ultrasonic technique allow inspections of the wave field at the surface of the structure only at specific inspection intervals. In contrast to this, applied, discrete sensors enable permanent monitoring of the structural health even during operation.

To gain additional information about the wave propagation inside the structure, a sensor can be integrated at the location of event. The authors presented an embeddable microelectromechanical sytem (MEMS) vibrometer made mainly out of borosilicate glass for GUW detection in a previous work [9]. However, when sensors are integrated, they cause a local stiffness change that results in a weakening of the structure and change of

 doi:10.20944/preprints202209.0075.v1

the acoustic impedance. As stated above, this affects the propagating wave field and the integrated sensor acts as a local defect. However, the separation of interference caused by sensors or damage is crucial for a reliable structural health monitoring system.

The characteristics of wave field interferences with damage are extensively investigated in literature. Typical types of damage are cracks, corrosion, impact, delaminations and through-holes. Within the classical approach, which is usually referred to as the linear wave propagation, the detection of damage smaller than the wavelength is not possible [10]. Due to this limitation over the last decades a second approach was profoundly investigated dealing with the nonlinear wave propagation. This approach is based on the generation of higher harmonic modes due to microstructural damage [11–14]. This effect is detectable within the linear wave propagation by a loss of energy recognizable in wavelet decomposition plots [15]. The work presented here focuses on sensor development and integration for the wave propagation detection or observation in fiber metal laminates. Typical damage scenarios in this context are severe delaminations due to low-velocity impact [16,17]. Since the size of these delaminations is typically at least within the range of the considered wavelength, only the linear wave propagation is analyzed here. The influence of delaminations and impact damage on the linear wave propagation has been profoundly investigated over the years [5,6,15,18–21]. It is shown that the scattered and converted mode amplitudes depend on the fiber orientation, the delamination size as well as the relative position along the laminate's height [6]. The amplitude increases with the delamination size [6,15,22], the time-of-flight is affected [15] and mode conversion occur [5]. Besides this, the wave field is also significantly influenced by through-holes [15], causing wave scattering [23]. In addition, the interaction of GUW with material discontinuities is investigated experimentally and numerically regarding welded joints of dissimilar materials [21]. The wave interaction is described by the definition of transmission and reflection coefficients and mode conversion is observed. Here, it is important to note, that the mode conversion is not only induced by damage, but is also strongly connected to the random distribution of the material parameters in fiber-reinforced composites (FRP) [24,25].

As shown, there is extensive work on the interference between damage and GUW whereas the influence of integrated sensors is hardly addressed. In contrast to discrete sensors, the integration of fiber Bragg grating (FBG) sensors is investigated profoundly in literature [26–28]. However, due to their geometry, the influence of FBG on the wave propagation is assumed to be negligible. Hence, the integration of discrete sensors requires more profound research and can be divided into attempts for single sensors and for sensor networks. Single sensors can be integrated quite well without affecting their performance and without weakening the structure substantially. This is investigated for three-point bending and fatigue tests and is confirmed in the presence of damage to the structure [29,30]. Another approach is the integration of full built-in sensor networks using flexible printed circuit board (PCB) layers with an applied network. They can be used as a whole layer during laminate layup [31,32].

There are multiple aims when integrating piezoelectric sensors into FRP. Integrated sensors or sensor networks can be used to monitor the curing of epoxy resin during manufacturing [32], damage evolution under cyclic load [33] or determining modes of failure such as matrix cracking, fiber matrix debonding, fiber breaking or delamination in FRP [29,34].

To evaluate a monitoring system with integrated sensors, the influence on the mechanical properties has to be taken into account. A lot of research addresses the integration of lead zirconate titanate (PZT) sensors in carbon fiber-reinforced polymer (CFRP). The integration of single sensors shows no influence on the fatigue strength [33], but the tensile and compressive modulus are reduced by approx. 21 % and 13 %, respectively [35]. A polyimide insulation layer reduces the compressive, flexural and interlaminar shear strength in CFRP specimens whereas a usage of small glass fiber-reinforced polymer (GFRP) samples as insulation did not [36]. The integration of a whole PCB layer with a PZT transducer network in CFRP only minimally influences the material properties of the laminate such as

 doi:10.20944/preprints202209.0075.v1

shear strength [32]. An investigation with graphite/epoxy laminates shows no effect on the tensile strength and Young's modulus when PZT actuators are embedded [37].

Although the integration of sensors shows no significant degradation of the structure's mechanical properties, a difference in performance between surface-bonded and embedded transducers might occur. A comparison of emitter-receiver combinations in GFRP shows, that configurations exist, where embedding both, emitter and receiver, gives the best signals even compared to two surface-bonded transducers [38]. This behaviour seems to depend strongly on the configuration of material, layup and frequency used as it could be shown, that sensors integrated into CFRP specimens show higher signal amplitudes for surface-mounted emitting transducers than for embedded ones [39]. This is supported by a further investigation on an integrated sensor network into CFRP. It demonstrates that the integrated sensor network shows little environmental noise as well as stable and repeatable data acquisition characteristics in comparison with surface-applied PZT sensors [40].

Experimental setups used to determine wave characteristics need defined boundary conditions and a wave field with as little disturbances as possible. Normally, the specimens are chosen to be as large as possible to avoid reflections from the edges and their superpositions with the signal of interest. However, large specimens increase the manufacturing effort, costs and material consumption. Narrow specimens avoid these drawbacks while showing a more complex wave field. The suitability of strip-like specimens to investigate GUW propagation is subject to current research. It was investigated, whether a narrow isotropic aluminum specimen could be simplified as a 1D structure and used to generate a straight wave front. The propagation of flexural and axial waves was numerically simulated in a 14 mm wide strip for the investigation of crack interaction. It showed straight wave fronts along the wave propagation direction but also an increasing dispersion and diminishing coherence when the signals superimpose with reflections from the strip's end [41]. Increasing the specimens width to e.g. 40 mm leads to amplitude variations along and across the specimen width indicating standing waves due to the superposition of reflected waves from the specimens edges [42]. A strategy to cope with this challenge is to use time gating to extract the relevant wave packages from the occuring reflections from the specimen's edges [43].

Summarizing, on the one hand, the literature review presents investigations on GUW interaction with damage. On the other hand, the performance of integrated discrete sensors for SHM applications using GUW is investigated. However, the influence of the sensor integration on the wave field has not been addressed yet. In addition, the geometry of a possible sensor is of interest. Subsequently, the aim of this paper is to investigate the influence of an embedded sensor, as presented by the authors [9], in GFRP on the propagating GUW field using narrow strip specimens to reduce the manufacturing effort.

In this work, it is shown that the integrated inlays cause reflections that cannot be experimentally detected and are therefore assumed not to influence the wave propagation significantly. However, reflections from the specimens' edges do occur and superimpose with the propagating waves. A method is presented to distinguish between these reflections and the interactions at the inlays using the periodic behaviour of the occurring wave packages.

Hence, this article is structured as follows: The materials and methods section starts with the design of the GFRP specimen with an integrated sensor inlay and an estimation of the related dispersion relation. The numerical model to deduce possible wave interactions between GUW and the inlay is presented. This is followed by an introduction of the experimental setups of the air-coupled ultrasonic technique and a 3D laser Doppler vibrometer (LDV) measurement. The methods section closes with a description of the continuous wavelet transformation (CWT) used to evaluate the experimental data. Afterwards, the numerical and experimental results are presented. Regarding the extracted B-scans of the measurement, possible reflections in the wave field are discussed. Subsequently, the CWT is used for time signal reconstruction to identify reflected wave packages. The work closes

Preprints (www.preprints.org) | NOT PEER-REVIEWED | Posted: 6 September 2022 doi:10.20944/preprints202209.0075.v1

with a discussion of the results including a critical analysis of the experimental procedures and a comparison between the numerical and experimental results.

2. Materials and Methods

2.1. Design of the Specimens

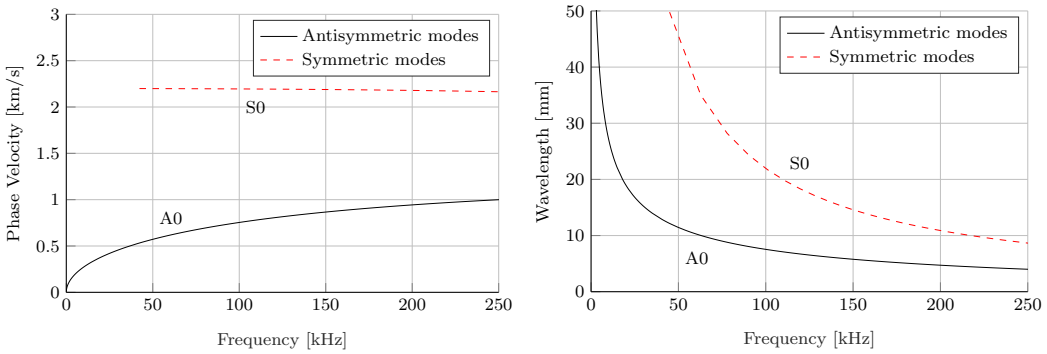

(a) Phase velocities of the fundamental modes. **(b)** Wavelengths of the fundamental modes.

Figure 1. Dispersion diagrams of the GFRP specimen under investigation. Material properties used can be found in Table 1.

For the design of the strip specimens, the unidirectional GFRP prepreg DLS1611 from Hexcel Corp. is used. The fiber orientation is chosen to be perpendicular to the strip specimen's length since the lower stiffness in this direction leads to smaller velocities. The aim is to selectively reduce the propagation velocities in the direction of the strip specimen's length by design. Regarding the analytically solved dispersion relations shown in Figure 1a and Figure 1b, the fundamental wave modes are expected to have a minimum wavelength of 3 mm and a maximum phase velocity of 2200 m/s. The material parameters assumed for the solution of the dispersion relation are standard values for unidirectional GFRP provided in Table 1.

Table 1. Material properties of the individual layers used i. a. in the numerical model.

Material	E_1 [GPa]	E_2 [GPa]	G_{12} [GPa]	G_{23} [GPa]	ν_{12} [-]	ρ [g/m^3]
GFRP DLS1611 (Hexcel Corp.)	54	9.4	5.55	3.75	0.33	1,980
Polyimide	2.5	2.5	1.52	1.52	0.34	1,420

Considering a possible integration of sensors into plate-like structures for SHM using GUW, a simplified approach is followed. As stated above, the sensors under investigation are MEMS vibrometers made mainly out of borosilicate glass [9]. As no sensing effect is needed, the sensor can be simplified by a bulk glass body made from the same material as the MEMS vibrometers themselves. In real-world applications, an electrical contacting of the sensor is needed. PCB based on polyimide substrates with conducting traces made from copper are state of the art for contacting electrical components. Therefore, the representative samples under investigation consist of a glass body (cf. Figure 3), representing the discrete sensor [9], which is adhesively bonded to a polyimide substrate, representing the PCB, using a high-temperature resistant cyanoacrylate, a typical bonding material.

Following this procedure, six different strip specimens are manufactured. Figure 2 illustrates an example of a strip specimen with polyimide inlay and applied square sensor body in plane and cross-sectional view. The strip specimens' height is approx. 2 mm built up by 16 prepreg layers with a nominal thickness of 0.12 mm each. Five out of six specimens have in common that a polyimide inlay is integrated. The polyimide inlay is 200 mm long, 2 mm wide and has a thickness of 25 µm. Among these five specimens, four additionally have differently shaped sensor glass bodies adhesively bonded on the end of the polyimide

Preprints (www.preprints.org) | NOT PEER-REVIEWED | Posted: 6 September 2022 doi:10.20944/preprints202209.0075.v1

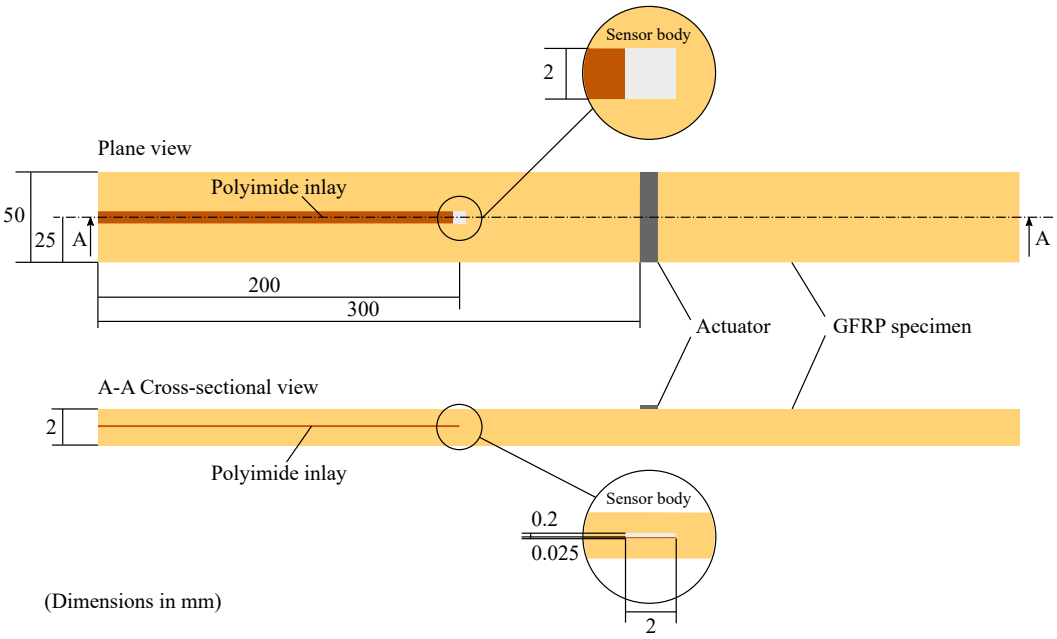

Figure 2. Sketch of the GFRP specimen design showing the dimensions, the polyimide inlay and an applied square dummy sensor body (cf. Figure 3) made out of the same borosilicate glass than the representative MEMS vibrometer [9] under investigation.

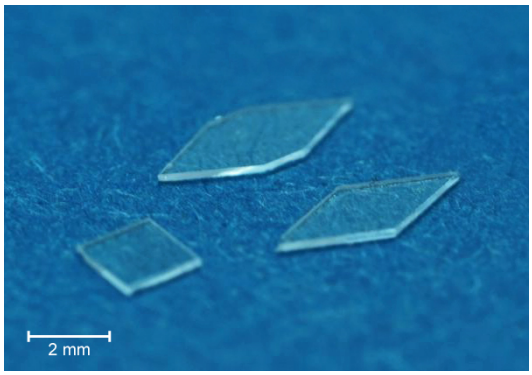

Figure 3. Glass sensor bodies as dummies for simulating the integration of a MEMS vibrometer [9] into a laminate. The glass inlays are made from BOROFLOAT33 borosilicate glass wafers with a thickness of 200 µm and shaped using a wafer-dicing saw.

inlay using cyanoacrylate. The cross section of the sensor bodies in wave propagation direction is 2 mm wide and 200 µm high. The different sensor shapes are shown in Figure 3. The aim is to investigate whether the sensor shape also influences the wave propagation behaviour. For GUW excitation, a PZT ceramic actuator is applied 100 mm away from the beginning of the inlay.

An overview of the specimens' inlay specifications is given in Table 2. A strip specimen example is shown in Figure 4.

Preprints (www.preprints.org) | NOT PEER-REVIEWED | Posted: 6 September 2022 doi:10.20944/preprints202209.0075.v1

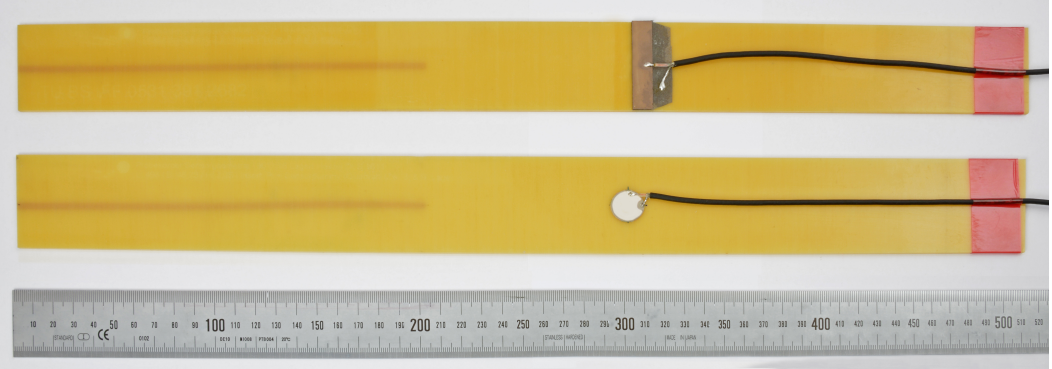

Figure 4. GFRP strip specimens with scale, visible polyimide inlay (orange, left) as well as rectangular (top) and circular (bottom) PZT actuators. For the exact dimensions and setup cf. Figure 2.

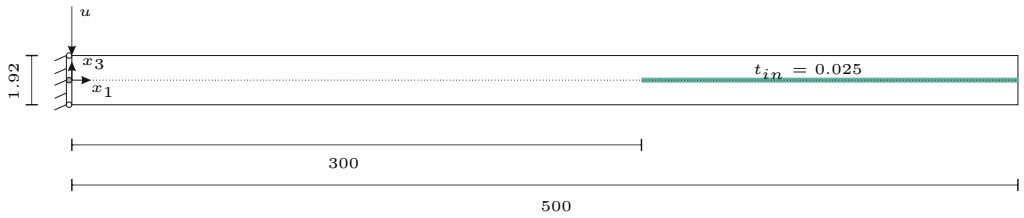

Figure 5. Sketch of the two-dimensional numerical model used to simulate the interaction between the GUW propagation and a polyimide inlay (green) integrated into a GFRP laminate. All measures in mm.

Table 2. Overview of the strip specimen configurations.

inlay type	position
no insert	-
polyimide / no sensor	8th / 9th layer (midplane)
polyimide / square	8th / 9th layer (midplane)
polyimide / rhombic	8th / 9th layer (midplane)
polyimide / flattened rhombic	8th / 9th layer (midplane)
polyimide / rhombic	12th / 13th layer

2.2. Numerical Simulation

To analyze the impact of sensor inlays on the GUW propagation without any experimental side effects, numerical simulations are carried out in a first step as a preliminary investigation. The numerical simulations are not meant to represent the subsequent experiments in their entirety, but to give a qualitative impression on what to expect during the LDV and air-coupled measurements.

For the finite element simulation, a two-dimensional model under plane strain assumption is used that represents the cross section of the specimen introduced in Section 2.1. To investigate the influence of the polyimide inlay on the wave propagation, two different waveguides are used. The first model represents a GFRP specimen without an inlay to observe the wave propagation in an undisturbed cross section. Following the stacking sequence provided in Section 2.1, the size of the numerical model is 500 mm $\times$ 1.92 mm with the fibers being orientated perpendicular to the wave propagation direction. The second model includes the polyimide inlay, indicated in green in Figure 5. The work presented here, focuses on the linear wave propagation. Therefore, inhomogeneities are only detectable, if their size is at least within the magnitude of the wavelength [10]. Due to this, the sensor body itself is not incorporated into the modeling procedure, because its overall size of 2 mm $\times$ 0.2 mm is smaller than the expected wavelength of the A_0-wave mode. The material properties of the components are provided in Table 1.

Preprints (www.preprints.org) | NOT PEER-REVIEWED | Posted: 6 September 2022 doi:10.20944/preprints202209.0075.v1

For the numerical simulation, the wave field is excited by a five-cycle Hanning windowed sine burst with a center frequency of 75 kHz, 120 kHz, and 200 kHz, respectively. The same signal is later used for the subsequent LDV-measurement. The excitation is realized by an out-of-plane displacement at the upper left corner of the numerical model. Furthermore, a symmetry boundary condition is applied to the left edge, cf. Figure 5. The distance between the excitation and the polyimide inlay is selected in such a way that the two fundamental modes A_0 and S_0 can be analyzed separately to gain a better understanding of the wave interaction with the inlay. All remaining boundary conditions are depicted in Figure 5.

To ensure correct simulations of the wave propagation in the composite, a sufficient spatial discretization $\Delta x_{\max}$ and time stepping $\Delta t_{\max}$ must be selected. Here, the following conditions apply [14,44]

$$\Delta t_{\max} = \frac{1}{20 f_{\max}}, \tag{1}$$

$$\Delta x_{\max} = \frac{\lambda_{\min}}{20}. \tag{2}$$

However, the discretization of the model depends not only on the wavelength of the wave modes, but also on the layered structure of the waveguide. Due to the thin polyimide layer in contrast to the overall specimen thickness, the selected element edge length is much smaller than the required value following Equation 2. Furthermore, a symmetric discretization is targeted. Therefore, the inlay is discretized with 2 elements over the thickness, whereas for the GFRP layers in total 40 elements are used. This leads to an almost equal vertical edge length of the elements over the thickness of the specimen. To further ensure an almost square shape of the elements, 10,000 second-order Lagrange elements are used alongside the specimen. Hence, in total 400,000 9-node-elements are used to form a structured mesh of the waveguide.

The numerical simulations are conducted in COMSOL Multiphysics. With the presented discretization, the computation time of the wave propagation in GFRP with a polyimide inlay takes approx. 6h.

2.3. Experimental Setup

To analyze the detectability of the wave interaction with the polyimide inlay in real specimens, two separate experimental procedures are performed. As in the numerical simulations, B-scans are extracted as representation of the wave field along the path from the actuator to the inlay. This method is performed for both experiments. In the first run, the wave propagation is measured using an air-coupled ultrasonic technique. All six specimens are examined with regard to a possible reflection phenomenon at the polyimide inlay. In a second run, a 3D-LDV measurement is used at different excitation frequencies for one specimen. The two different measurement procedures allow the experimental separation and evaluation of the different displacement field components. Details of the two procedures are described in the following.

2.3.1. Measurements of GUW Using the Air-Coupled Ultrasonic Technique

The air-coupled ultrasonic technique used in this first measurement is known as an established method in non-destructive testing. It uses an applied actuator on the structure's surface instead of a test probe [8]. The frequencies of the structure's sound radiation can be detected by microphones which are sensitive to a narrowband frequency range and need to be chosen referring to the structure's excitation frequency. As done in the numerical simulations, the chosen frequencies are 75 kHz, 120 kHz and 200 kHz. Following this, the used microphones for the detection are AirTech 75, AirTech 120 and AirTech 200.

A variation of the probe angle allows the detection of different components of the excited wave modes. Therefore, two probe angles are chosen: probe perpendicular to the strip specimens and a probe angle of approx. 10° to the vertical. Using the probe perpendicularly

Preprints (www.preprints.org) | NOT PEER-REVIEWED | Posted: 6 September 2022 doi:10.20944/preprints202209.0075.v1

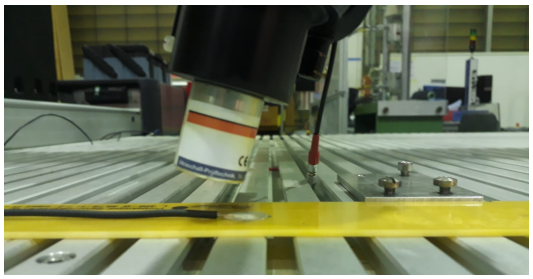

Figure 6. Variation of the probe angle of the air-coupled detection. The inclination additionally enables the detection of in-plane proportions compared to a perpendicular setup, which is only sensitive to out-of-plane components.

allows the detection of the pure out-of-plane component of the displacement field, while using the probe under a certain angle detects a superposition of out-of-plane and in-plane components of the propagating waves.

The recorded microphone signals are filtered by a bandpass of 12th order with a chosen bandwidth from 0.5 times to 1.5 times the burst center frequency using receiver amplification factors from 31.5 dB to 43.5 dB. All measurements are averaged eight times.

A round PZT ceramic (material: PIC255) with a diameter of 16 mm and a thickness of 0.2 mm is used as an actuator. The excitation signal is a three-cycle Hanning windowed rectangular burst signal with the named frequencies for all six strip specimens. Although it shows a wider bandwidth of excitation frequencies, it contains the same center frequency as a sinusoidal burst and hence, gives comparable signals. Increasing excitation frequencies lead to a decrease in the amplitude of the measured signals due to material damping effects. Therefore, the amplification of the excitation signals must be adjusted. For the three measurements, excitation voltages from 35.5 V to 50.2 V are used.

The measuring path is 235 mm long, which corresponds to the distance between the PZT ceramic and the strip specimen's end. Hence, it covers the path between the actuator and the polyimide inlay. The distance between the actuator and the beginning of the polyimide inlay is 100 mm. That means that reflections caused by the inlay are expected to occur in the extracted B-scan after 100 mm of path length.

2.3.2. Measurements of GUW Using the LDV

The aim of the 3D LDV measurement is the extraction of the in-plane and out-of-plane component of the wave propagation to allow a separate evaluation [4] and a better comparability to the numerical results.

The procedure is as follows: before the measurements, a rectangular actuator replaces the round PZT ceramic on the strip specimen with the polyimide inlay without additional sensor body according to Figure 4. The actuator is as wide as the strip, 10 mm long and 0.2 mm high. The rectangular ceramic (material: PIC255) is chosen to avoid early reflections in the wave field due to the radially symmetric wave fields propagating from the round PZT ceramics. The intention is to create a straight wave front propagating in the strip specimen before superimposing with reflections from the specimens' edges.

The measurement path is 110 mm long and positioned in the middle of the strip specimen inline with the polyimide inlay. The distance between the start of the measurement path and the beginning of the polyimide inlay is 90 mm. This means that possible reflections would be visible at a path length of 90 mm in the later extracted B-scans. Retroreflective foil is applied to the specimen's surface along the measurement path to increase the signal quality of the LDV measurement.

In the experimental investigations, 250 equidistant measurement points along the measurement path are used, offering a spatial resolution of 0.44 mm. This corresponds to six points per minimal expected wavelength, cf. Figure 1b.

In reference to the simulation described in Section 2.2 and the air-coupled-measurements described in the Section 2.3.1, the chosen frequencies for the experiment are 75 kHz, 120 kHz,

 doi:10.20944/preprints202209.0075.v1

and 200 kHz. The excitation signal is a five-cycle Hanning windowed sine burst signal. Three measurements are performed under different angles and a coordinate transformation is implemented to decompose the measured surface velocities into one out-of-plane and two in-plane components [4,45].

2.4. Fundamentals of the Continuous Wavelet Transformation

A wavelet transformation offers the possibility to extract information about the occuring frequencies in a time signal over a localization in the time-domain. Hence, it is a method of direct time-frequency analysis, which works using a time-limited window with an average amplitude of zero and a variable size [2]. A single wavelet function is the basis for the wavelets constructed by translation and dilation. The location of the wavelet in the time domain is defined by a scaling and a translation parameter [46]. The transformation's resolution at different times and frequencies is governed by the Heisenberg uncertainty principle [46]. There are a variety of wavelets that are selected depending on the application and the time signal's characteristics.

A CWT of a time signal leads to a representation of the energy distribution per frequency in the time-domain [2]. Since the discussed signals in this work are not continuous but change the instantaneous frequency within a certain range of time, a fixed window-size, as e. g. in the short-time fourier transformation (STFT), might lead to a loss of information. In comparison to the STFT, the CWT offers a variable window size and therefore, a higher precision simultaneously in both the time- and frequency-domain [2]. A CWT can also be undertaken in the spatial-domain, which leads to occurring wavenumbers over the spatial resolution instead of occurring frequencies over the time-scale.

In this study, the experimental time signals are filtered using the CWT in the time-frequency domain. They are reconstructed using the inverse CWT with a narrower frequency bandwidth set to $\pm$ 5 kHz around the burst center frequencies to remove discontinuities that cause dissipation in the spectra. This helps to identify wave packages better. Afterwards, the spatial CWT is performed. This is done to identify where the different wavelengths corresponding to the two fundamental modes occur spatially. The identification of wave packages can be deduced by the appearance of a specific mode's wavelength in a position in space and time. These steps are undertaken for the measurements of all three frequencies. The temporal and spatial CWT are performed using the analytic Morse wavelet. The symmetry parameter is set to 3 and the time-bandwidth product is 60. 10 voices per octave are used [47].

3. Results

3.1. Numerical Results

The results of the numerical simulations are provided in Figures 7 and 8. To generate the depicted B-scans, the time signals are vertically aligned for each observation point along the specimen. The result is a surface plot, where the amplitude of the wave propagation is plotted over the propagation direction (horizontal axis) and time (vertical axis). Figure 7 presents B-scans of the in- and out-of-plane displacement component for the wave propagation in a pure GFRP waveguide (Figures 7a and 7c) and a waveguide with a polyimide inlay (Figures 7b and 7d) at 120 kHz. In both cases, two wave modes are excited; the fundamental S_0- and A_0-mode. The divergence of the A_0-mode with the propagation distance is caused by its strong dispersive nature. This can be derived from the dispersion diagram, cf. Figure 1a. Comparing the in- and out-of-plane displacement component for the GFRP waveguide reveals, that the in-plane displacement component of the S_0-mode is dominant over the out-of-plane component, whereas for the A_0-mode the out-of-plane component is dominant. This fits the characteristics of GUW in thin-walled structures [48]. Inserting an inlay into the structures causes reflections of the two wave modes at the impedance change. First, the S_0-mode passes the change of the cross section, which leads to a partial reflection of the wave mode, indicated by an additional wave package which propagates back to the excitation point with the same absolute slope. However, this is only

Preprints (www.preprints.org) | NOT PEER-REVIEWED | Posted: 6 September 2022 doi:10.20944/preprints202209.0075.v1

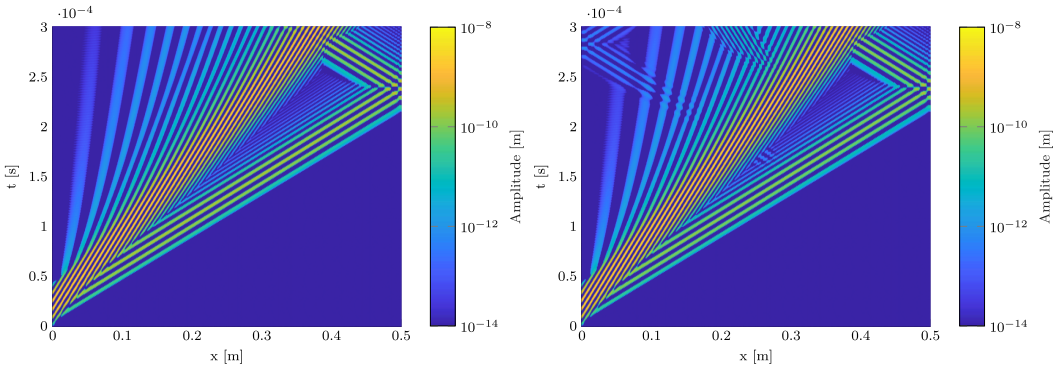

(a) Wave field without polyimide inlay, in-plane displacement field.

(b) Wave field with polyimide inlay, in-plane displacement field.

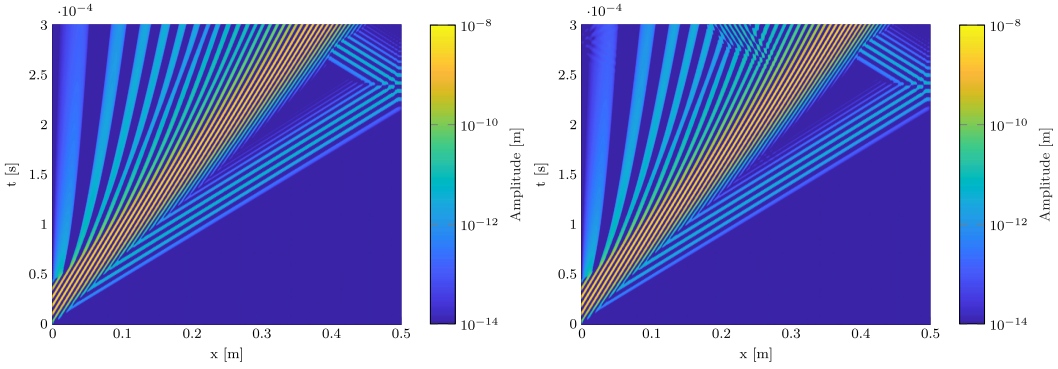

(c) Wave field without polyimide inlay, out-of-plane displacement field.

(d) Wave field with polyimide inlay, out-of-plane displacement field.

Figure 7. Comparison of the numerically determined wave propagation in a pure GFRP laminate and a waveguide including a polyimide inlay in the midplane at a burst center frequency of 120 kHz using a B-scan representation. The polyimide inlay starts at 0.3 m (cf. Figure 5).

Preprints (www.preprints.org) | NOT PEER-REVIEWED | Posted: 6 September 2022 doi:10.20944/preprints202209.0075.v1

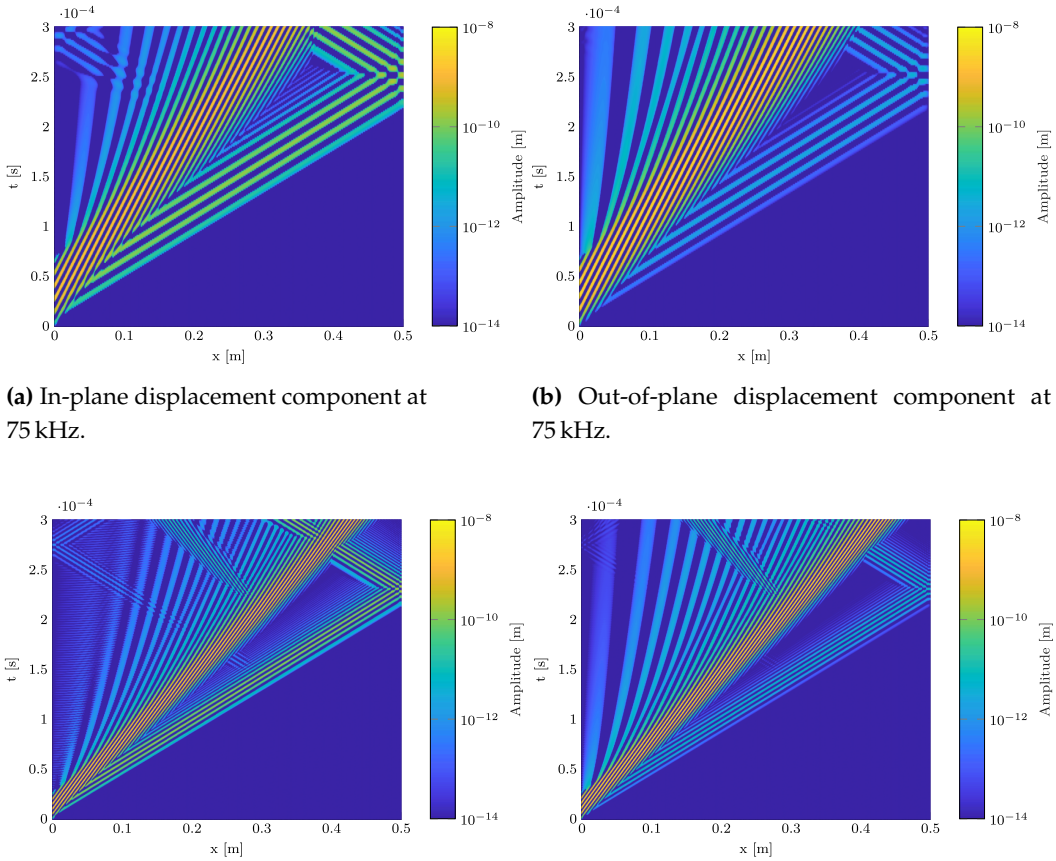

(a) In-plane displacement component at 75 kHz.

(b) Out-of-plane displacement component at 75 kHz.

(c) In-plane displacement component at 200 kHz.

(d) Out-of-plane displacement component at 200 kHz.

Figure 8. Comparison of the numerically determined wave interaction of GUW with the polyimide inlay in the midplane of the GFRP specimen at different burst center frequencies. The design of the numerical model is depicted in Figure 5.

detectable in the in-plane displacement field. For the out-of-plane motion, the interaction is only hardly observable. In the upper left corner, a slight disturbance is recognizable in the A_0-mode, which meets the characteristics of the partially reflected S_0-mode in Figure 7b. After the S_0-mode passed the cross section change, the A_0-mode interacts with the inlay. The partially reflected A_0-mode is clearly detectable in both displacement components.

To get deeper insights of the inlay influence on the wave propagation, Figure 8 gives the results of numerical simulations at the remaining frequencies of 75 kHz and 200 kHz. Again, both displacement field components are provided for each simulation. The same conclusion can be derived from Figures 8a and 8b (75 kHz) as well as Figures 8c and 8d (200 kHz). Beside the signal at 75 kHz, the interaction of both fundamental wave modes are clearly detectable in the in-plane displacement component, whereas the out-of-plane component reveals only the partially reflection of the A_0-mode. For 75 kHz, due to the high wavelength, the signal is not long enough to also capture the reflected A_0-mode.

In conclusion, the interaction of the excited GUW with the polyimide inlay is found for a certain frequency range. Both, the fundamental A_0- and S_0-mode interact with the inlay. However, it is important to note, that the resulting amplitude is more than one order of magnitude smaller than the amplitudes of the excited wave modes. Due to this reason, the B-scans are plotted with a logarithmic amplitude scale. For an experimental validation, the main focus is set on the in-plane displacement, since the interaction of the S_0-mode is properly detectable.

Preprints (www.preprints.org) | NOT PEER-REVIEWED | Posted: 6 September 2022 doi:10.20944/preprints202209.0075.v1

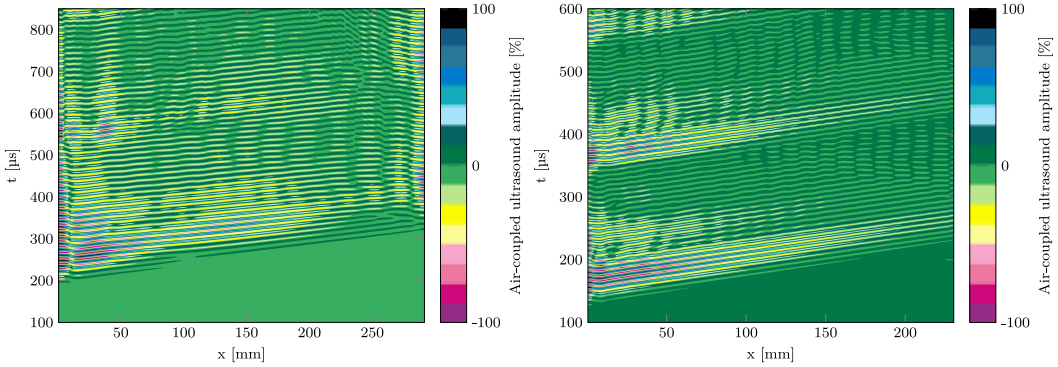

(a) 75 kHz with perpendicular probe.

(b) 120 kHz with perpendicular probe.

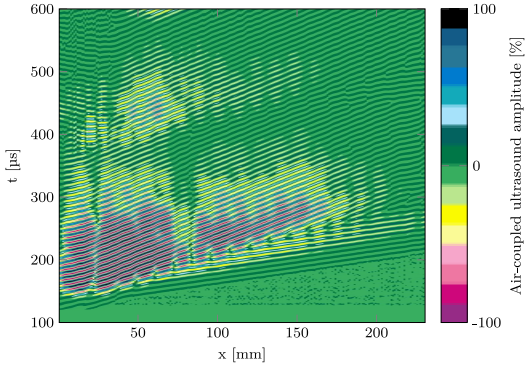

(c) 120 kHz with probe under an angle of 10°.

Figure 9. Experimentally determined B-scan of the GFRP strip specimen along the measurement path from actuator to polyimide inlay. Generated using air-coupled ultrasound technique. The polyimide inlay starts at x =100 mm (cf. Figure 2). The measurement with inclined probe shows two modes while the experiment with a perpendicular probe only reveals one mode which is due to the different sensitivities for in-plane and out-of-plane components and the different occurring displacement fields.

3.2. Evaluation of the Air-Coupled Measurements

B-scans are extracted for all measurement paths. Exemplary for all measurements and in reference to the numerical simulations described in Section 3.1, the following scans are presented in this paper: B-scan of the strip specimen with polyimide inlay at 75 kHz with perpendicular probe in Figure 9a, B-scan of the strip specimen with polyimide inlay at 120 kHz with perpendicular probe in Figure 9b, and B-scan of the strip specimen with polyimide inlay at 120 kHz with a probe angle of approx. 10° in Figure 9c. As visible in Figure 9c, two wave fronts occur which means that under an angle of the probe both, the slower A_0- and the faster S_0-mode can be detected. In the B-scans of the measurements with the perpendicular probe, only the S_0-mode can be detected. All together, 36 scans are recorded for three excitation frequencies, two probe angles, and six strip specimens.

It is evident, that the measurements by the air-coupled technique do not show any visible reflections at the polyimide inlay whether a glass sensor body is applied or not. This finding is independent from whether the scans of the waves' displacement field contain pure out-of-plane wave motion or superimposed in-plane and out-of-plane motion. This leads to the conclusion that a separate investigation of the in-plane and out-of-plane component of the wave field is necessary to allow a more accurate comparison with the simulations. Additionally, the glass sensor body is neglected for the following investigations referring to the model assumptions in Section 2.2.

Preprints (www.preprints.org) | NOT PEER-REVIEWED | Posted: 6 September 2022 doi:10.20944/preprints202209.0075.v1

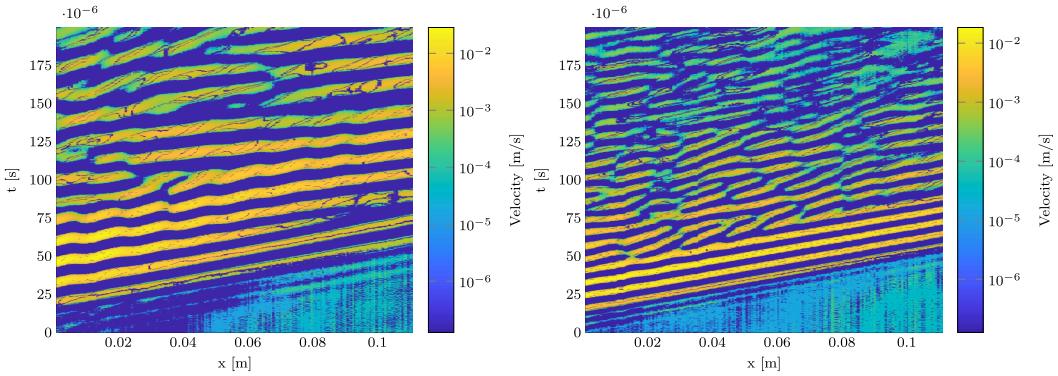

(a) 75 kHz. **(b)** 120 kHz.

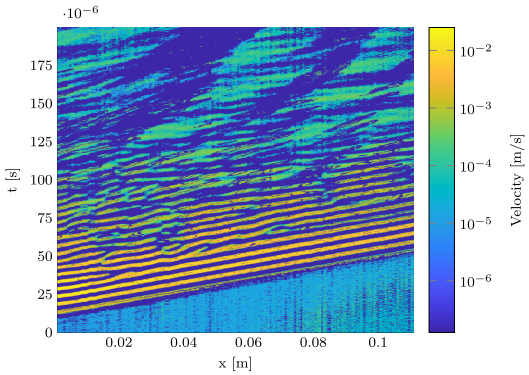

(c) 200 kHz.

Figure 10. Experimentally determined B-scan of the GFRP strip specimen along the measurement path from actuator to polyimide inlay. The polyimide inlay starts at 0.09 m as the measurement path starts 0.01 m away from the actuator (cf. Figure 2). In-plane component, generated using 3D LDV measurement.

3.3. Evaluation of the 3D Measurements Using the LDV

Figures 10a to 10c hold the B-scans of the in-plane velocity component of the wave propagation. Again, a logarithmic amplitude scale is chosen. The fundamental A_0- and S_0-modes can be identified in all three B-scans.

The wave propagation speed of the S_0-mode can be derived from the slope in the B-scan as no significant dispersion occurs in this frequency range, cf. Figure 1a. As shown in Table 3, wave speeds could be identified that suit fairly well the dispersion diagram of the phase velocity in Figure 1a and indicate a slightly decreasing velocity with an increasing frequency regarding the S_0-mode. Deviations between experimental and simulative results are mostly due to the assumption of erroneous material properties in the dispersion diagram generation, as no material data sheet from the manufacturer is available.

Table 3. Phase velocity identification for the fundamental S_0-modes.

burst center frequency [kHz]	$\mathbf{c_{phase,exp,LDV}(S_0)}$ [m/s]	$\mathbf{c_{phase,sim}(S_0)}$ [m/s]
75	2,682	2,197
120	2,500	2,193
200	2,444	2,179

It can be seen in all figures that no reflections at the polyimide inlay can be identified. Instead, wave packages occur that cannot be directly linked to the propagating A_0- and S_0-mode. In addition, the location of their occurrence cannot be explained by reflections at the specimens' end. The amplitudes of these reflections occur in the order of magnitude of the S_0-mode and the slope of the wave packages suggests that the reflection is another S_0-mode.

Preprints (www.preprints.org) | NOT PEER-REVIEWED | Posted: 6 September 2022 doi:10.20944/preprints202209.0075.v1

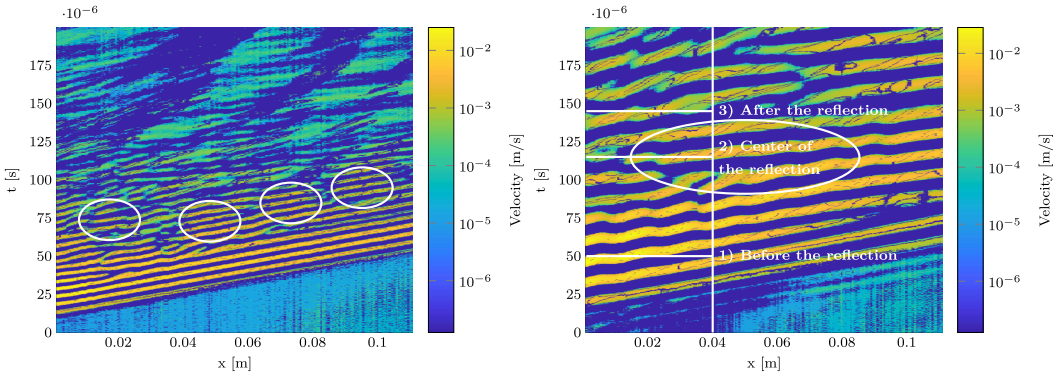

(a) 200 kHz. **(b)** 75 kHz.

Figure 11. Marked periodic reflections of the S_0-mode in the B-scan generated using 3D LDV measurement.

At 200 kHz, four wave packages can be identified showing the velocity of the S_0-mode. They are marked with white circles in Figure 11a. An overview of their precise position in the spatial and time domain is given in Table 4. The first wave package occurs due to near field effects near the actuator, since it is a bit shifted compared to the three other wave packages. The three wave packages afterwards show a clear periodic behavior without any shift.

The wave packages' variation of amplitude along the B-scans can be explained by the periodic superposition of forth and back running waves between the narrow edges of the specimen causing standing waves superposing the GUW. This will be verified in the following sections using a continuous wavelet transformation to distinguish these edge reflections from possible reflections at the polyimide inlay.

Table 4. Location of periodic wave reflections at 200 kHz (cf. Figure 11a).

wave package	spatial starting point [mm]	temporal starting point [ms]
1	15	0.075
2	40	0.07
3	65	0.08
4	90	0.09

3.4. Reconstruction of the Time Signals and Spatial CWT

In this section, the in-plane component of the displacement field in wave propagation direction perpendicular to the fibers is extracted from the 3D-LDV measurement. The in-plane component is selected as it shows best reflection visibility in the numerical results in Section 3.1. Referring to Section 2.3.2, the inlay-related reflections are to be expected at a position of 90 mm in the B-scan. However, the B-scans in Section 3.3 do not show reflections at this position. For the evaluation of the experimental data, a temporal and spatial CWT is performed as described in Section 2.4.

Since the S_0-mode shows a higher in-plane component than the A_0-mode, the former is used for further evaluation. It is investigated if the wavelength of the S_0-mode appears in the identified periodically occurring wave packages as this would be a proof of the reflection of the fast S_0-mode from the strip specimen's width. For this purpose, for each excitation frequency, the first reflected wave package is located in space and time in the B-scan. Three points in time are chosen starting from the location of the center of the wave package: a time before the reflected wave package occurs, one in the wave package's center and one after the wave package has decreased. This is exemplary shown for 75 kHz in Figure 11b. An overview over the times and the location for all three excitation frequencies is given in Table 5. Enclosed areas of vanishingly small amplitude in the spatial CWT can

Preprints (www.preprints.org) | NOT PEER-REVIEWED | Posted: 6 September 2022 doi:10.20944/preprints202209.0075.v1

be explained by destructive interference phenomena by superposing reflections. In the following, the results for all three measurements are presented.

Table 5. Points in time used to identify the first reflected wave packages with a spatial CWT evaluation.

burst center frequency	**temporal point**		
[kHz]	before reflection [µs]	center of reflection [µs]	after reflection [µs]
75	50	115	145
120	50	75	95
200	60	70	90

75 kHz

The results of the spatial CWTs for 75 kHz and the points in time defined in Table 5 are shown in Figures 12a to 12c. According to Figure 11b a location of 40 mm is under investigation, cf. dashed white line in Figure 12a. The spectra obtained using the CWT for all three points in time are investigated for occurring wavelengths corresponding to the two fundamental wave modes.
At 40 mm and 50 µs, the S_0- and A_0-mode start to diverge. At this location and this point in time, no reflections occur yet, cf. Figure 11b. The presence of both wave modes is shown in the spatial CWT as derived in Figure 12a. Taking into account a certain kind of uncertainty due to the transformation caused by the assignment between the spatial domains and the propagation properties, two horizontal peak branches are visible at wavelengths of approx. 10 mm and at approx. 30 mm. The occurring wavelengths fit well to the numerically derived values indicated with horizontal dashed white lines.

Figure 12b shows the CWT of the time signal in the temporal center of the reflection. According to the group velocities, the S_0-mode should have already passed. However, two low intensity branches can be identified for wavelengths corresponding to both the S_0- and A_0-mode. Straight wave fronts no longer occur due to the reflections from the specimen's edges. Different angles of incidence through the measuring path occur and distort the waves in the analysis. An increase in wavelength is to be expected. Due to the transformation-related uncertainty, the transitions of the branches in the diagram do not appear in clear delineation. However, both modes occur. As the S_0-mode appears as well, this indicates the presence of an S_0-mode reflection at the strips edges.

Figure 12c depicts the CWT for a point in time after the reflected wave package. A high intensity branch at a wavelength of approx. 12 mm occurs and remains visible at 40 mm. However, the S_0 branch at approx. 25 mm does not occur which confirms the non-appearance of the S_0-mode after the periodically appearing reflection wave package. In the following, the wavelengths in one point in time will be shown in the center of the first identified reflected wave package for 120 kHz and 200 kHz as listed in Table 5 .

120 kHz

At an excitation of 120 kHz, the first reflected wave package in the B-scan of the in-plane component is identified between 10 mm and 25 mm at 65 µs to 85 µs. In this time range, an appearance of the S_0-mode is not expected, because the propagating mode has already passed the location and the A_0-mode starts to appear. As visible in Figure 12d, the CWT at 75 µs shows both wave modes in two branches over a wide spatial range. The continuous appearance of the S_0-branch is an indication for reflections from the strip specimen's width. The maximum of amplitude at the end of the strip specimen can be explained by the excited wave package passing by before getting reflected at the strip specimens end.

Preprints (www.preprints.org) | NOT PEER-REVIEWED | Posted: 6 September 2022 doi:10.20944/preprints202209.0075.v1

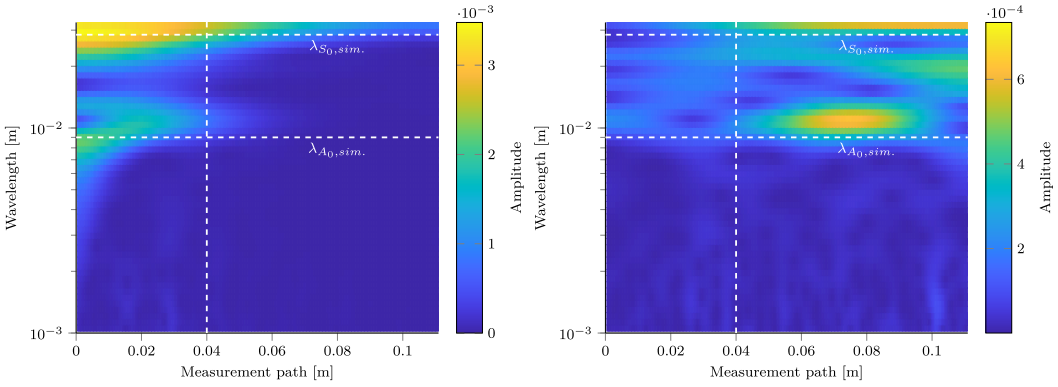

(a) 75 kHz and 50 µs (cf. Figure 11b).

(b) 75 kHz and 115 µs (cf. Figure 11b).

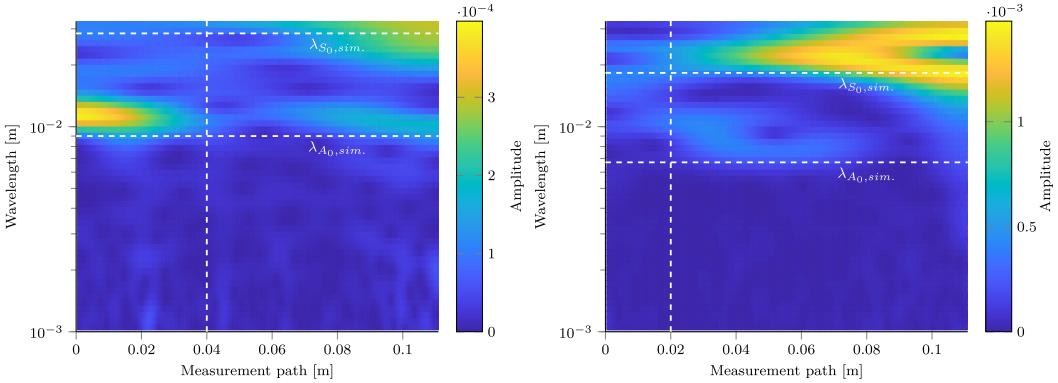

(c) 75 kHz and 145 µs (cf. Figure 11b).

(d) 120 kHz and 75 µs (cf. Figure 10b).

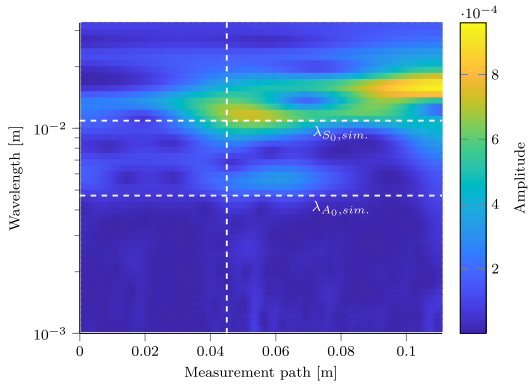

(e) 200 kHz and 70 µs (cf. Figure 10c).

Figure 12. Spatial CWT of the 3D-LDV measurements at time steps as stated in Table 5. Horizontal dashed lines indicate the wavelengths λ from the dispersion diagrams. Vertical dashed lines indicate locations of interest of identified wave packages in the B-scans.

 doi:10.20944/preprints202209.0075.v1

200 kHz

As shown in Figure 11a, the periodically repeating wave packages start at approx. 45 mm. The center of the wave package in the time domain is at 70 µs. At 90 µs, the wave package decreases and it is not to be expected that the wavelength of the S_0-mode occurs in the spatial CWT. Points in time smaller than 70 µs are expected to show the wavelengths of both fundamental modes in their spatial CWT. As Figure 12e shows at 70 µs, at a position of 45 mm, the wavelength of the S_0-mode occurs with a relatively high intensity peak covering the spatial range, in which the three reflected wave packages occur, while the A_0-mode shows with low amplitude at a position of 50 mm. Therefore, the occurrence of significant reflections of the S_0-mode is evident.

For all frequencies, a CWT can be used to show that the periodically occurring wave packages have the wavelengths of the S_0-mode. Taking into account the wave packages' location in space and time, this finding proves the superimposing reflections from the specimens' edges and that these can be distinguished from possible reflections at the polyimide inlay.

4. Discussion

The aim of this work is to investigate the influence of a thin and narrow polyimide inlay serving as substrate for a PCB with applied glass sensor body on the propagation of GUW in narrow GFRP specimens.

Preliminary numerical simulations of a GFRP specimen are done using a damping-free two-dimensional model. The simulations show that reflections of the S_0-mode do theoretically occur at the inlay but are at least an order of magnitude smaller than the excited S_0-mode.

Different experiments are performed to investigate whether these simulated reflections are detectable and of importance in a real-world application. For this purpose, an air-coupled ultrasonic technique is used, which provides superimposed information from the wave's displacement field. A subsequent 3D-LDV measurement allows a separation of the in-plane component of the displacement field and a direct comparison with the simulation. Air-coupled measurements are undertaken under excitation of round PZT ceramics. Due to the radial symmetric wave propagation field around the actuator, time delayed reflections from the specimens' edges occur and superimpose with each other. However, independently of the sensor body's shape, no reflections are detected. In a subsequent experiment, a GFRP strip specimen is excited by a rectangular PZT ceramic and the wave field is detected using a 3D-LDV measurement to extract the pure in-plane component, for which the numerical simulation predicts the highest reflections. Again, no reflections from the inlays are identified in the experiment.

However, periodically appearing wave packages are detected. The reconstruction of the measured time signals reversing the measurements' CWT as well as a subsequent spatial CWT show that the identified wave packages at the allocated points in time and space are indeed edge reflections of the S_0-mode.

Since reflections from the specimens' edges can be clearly identified due to their localization in space and time and since they show a clear periodical behaviour, they can be distinguished from possibly detectable inlay reflections.

Therefore, the GUW experiments and methods used can be successfully performed in the narrow GFRP specimens at hand.

As no reflections at the polyimide inlay can be experimentally identified in the specimen, it is concluded that material damping effects by the epoxy resin occur so intensely that reflections are damped below the detection threshold in the experiments. In contrast to the polyimide inlay, the sensor bodies are smaller than the occurring wavelengths in the experiment. Thus, it is reasonable that any possible sensor body shape applied to the polyimide inlay presented can be neglected for later GUW field experiments in the specimens presented when assuming the concept of linear wave propagation.

In conclusion, it can be experimentally shown, that thin and narrow polyimide inlays with applied MEMS vibrometers made out of glass for GUW detection in pure GFRP do not cause detectable reflections of GUW.

Author Contributions: Conceptualization, L.R., N.R.; methodology, L.R., N.R.; software, L.R., N.R., A.M.; validation, L.R., N.R., T.R.; formal analysis L.R., N.R.,T.R.,J.N.H., A.M.; investigation, L.R., N.R. T.R, J.N.H.; resources L.R., N. R., T.R., A.M., J.N.H.; data curation,L.R., T.R., N.R.; writing—original draft preparation, L.R., N.R.; writing—review and editing, T.R., J.N.H., N.R., L.R.; visualization, L.R.,T.R., N.R.; supervision, M.S.; project administration, M.S.; funding acquisition, M.S., R.L., A.D, N.R. All authors have read and agreed to the published version of the manuscript.

Funding: We expressly acknowledge the financial support for the research work on this article of the Research Unit 3022 "Ultrasonic Monitoring of Fibre Metal Laminates Using Integrated Sensors" (Project number: 418311604) by the German Research Foundation (Deutsche Forschungsgemeinschaft (DFG)). We also acknowledge support by the Open Access Publication Funds of Technische Universität Braunschweig.

Institutional Review Board Statement: Not applicable.

Informed Consent Statement: Not applicable.

Data Availability Statement: The raw data of the experiments can be requested from the authors.

Conflicts of Interest: The authors declare no conflict of interest. The funders had no role in the design of the study; in the collection, analyses, or interpretation of data; in the writing of the manuscript, or in the decision to publish the results.

References

1. Giurgiutiu, V. Structural health monitoring with piezoelectric wafer active sensors; Academic Press/Elsevier: Amsterdam, 2008.
2. Su, Z.; Ye, L., Eds. Identification of damage using Lamb waves: From fundamentals to applications; Vol. 48, Lecture notes in applied and computational mechanics, Springer-Verlag: Berlin, 2009.
3. Balageas, D.; Fritzen, C.P.; Güemes, A. Structural Health Monitoring; ISTE Ltd and ISTE: London and Newport Beach, CA, 2006. https://doi.org/10.1002/9780470612071.
4. Lammering, R.; Gabbert, U.; Sinapius, M.; Schuster, T.; Wierach, P., Eds. Lamb-Wave Based Structural Health Monitoring in Polymer Composites; Research Topics in Aerospace, Springer International Publishing: Cham, 2018. https://doi.org/10.1007/978-3-319-49715-0.
5. Guo, N.; Cawley, P. The interaction of Lamb waves with delaminations in composite laminates. The Journal of the Acoustical Society of America **1993**, 94, 2240–2246. https://doi.org/10.1121/1.407495.
6. Pudipeddi, G.T.; Ng, C.T.; Kotousov, A. Mode Conversion and Scattering of Lamb Waves at Delaminations in Composite Laminates. Journal of Aerospace Engineering **2019**, 32, 04019067. https://doi.org/10.1061/(ASCE)AS.1943-5525.0001060.
7. Mallet, L.; Lee, B.C.; Staszewski, W.J.; Scarpa, F. Structural health monitoring using scanning laser vibrometry: II. Lamb waves for damage detection. Smart Materials and Structures **2004**, 13, 261–269. https://doi.org/10.1088/0964-1726/13/2/003.
8. Schmidt, D. Modenselektive Übertragung von Lambwellen in Faserverbundstrukturen: Dissertation; Vol. 24, DLR-Forschungsbericht 2014, Deutsches Zentrum für Luft- und Raumfahrt e.V.: Braunschweig, 2014.
9. Haus, J.N.; Rittmeier, L.; Roloff, T.; Mikhaylenko, A.; Bornemann, S.; Sinapius, M.; Rauter, N.; Lang, W.; Dietzel, A. Micro-Oscillator as Integrable Sensor for Structure-Borne Ultrasound. Engineering Proceedings **2021**, 10. https://doi.org/10.3390/ecsa-8-11313.
10. Lissenden, C.J.; Liu, Y.; Choi, G.W.; Yao, X. Effect of Localized Microstructure Evolution on Higher Harmonic Generation of Guided Waves. Journal of Nondestructive Evaluation **2014**, 33, 178–186. https://doi.org/10.1007/s10921-014-0226-z.
11. de Lima, W.; Hamilton, M.F. Finite-amplitude waves in isotropic elastic plates. Journal of Sound and Vibration **2003**, 265, 819–839. https://doi.org/10.1016/S0022-460X(02)01260-9.
12. Deng, M.; Pei, J. Assessment of accumulated fatigue damage in solid plates using nonlinear Lamb wave approach. Applied Physics Letters **2007**, 90, 121902. https://doi.org/10.1063/1.2714333.
13. Pruell, C.; Kim, J.Y.; Qu, J.; Jacobs, L.J. Evaluation of plasticity driven material damage using Lamb waves. Applied Physics Letters **2007**, 91, 231911. https://doi.org/10.1063/1.2811954.
14. Rauter, N.; Lammering, R.; Kühnrich, T. On the detection of fatigue damage in composites by use of second harmonic guided waves. Composite Structures **2016**, 152, 247–258. https://doi.org/10.1016/j.compstruct.2016.05.049.
15. Kessler, S.S.; Spearing, S.M.; Soutis, C. Damage detection in composite materials using Lamb wave methods. Smart Materials and Structures **2002**, 11, 269–278. https://doi.org/10.1088/0964-1726/11/2/310.
16. Chai, G.B.; Manikandan, P. Low velocity impact response of fibre-metal laminates – A review. Composite Structures **2014**, 107, 363–381. https://doi.org/10.1016/j.compstruct.2013.08.003.

17. Morinière, F.; Alderliesten, R.; Tooski, M.; Benedictus, R. Damage evolution in GLARE fibre-metal laminate under repeated low-velocity impact tests. Open Engineering **2012**, 2, 603–611. https://doi.org/10.2478/s13531-012-0019-z.
18. Zheng, K.; Li, Z.; Ma, Z.; Chen, J.; Zhou, J.; Su, X. Damage detection method based on Lamb waves for stiffened composite panels. Composite Structures **2019**, 225, 111137. https://doi.org/10.1016/j.compstruct.2019.111137.
19. Burkov, M.V.; Eremin, A.V.; Byakov, A.V.; Lyubutin, P.S.; Panin, S.V. Impact Damage Detection in Laminate and Honeycomb CFRPs using Lamb Wave Ultrasonic Sensing. Russian Journal of Nondestructive Testing **2021**, 57, 114–124. https://doi.org/10.1134/S1061830921020042.
20. Sharif-Khodaei, Z.; Aliabadi, M.H. Lamb-Wave Based Damage Detection in Anisotropic Composite Plates. Key Engineering Materials **2014**, 627, 1–4. https://doi.org/10.4028/www.scientific.net/KEM.627.1.
21. Fakih, M.A.; Mustapha, S.; Harb, M.; Ng, C.T. Understanding the interaction of the fundamental Lamb-wave modes with material discontinuity: finite element analysis and experimental validation. Structural Health Monitoring: An International Journal **2021**, p. 147592172110071. https://doi.org/10.1177/14759217211007118.
22. Singh, G.; Aggarwal, A.; Kumar, S.; Kalra, S. Delamination Detection and Evaluation in Composite Laminates Using Guided Ultrasonic Waves. In Recent Trends in Industrial and Production Engineering; Dubey, A.K.; Sachdeva, A.; Mehta, M., Eds.; Lecture Notes in Mechanical Engineering, Springer Singapore: Singapore, 2022; pp. 47–56. https://doi.org/10.1007/978-981-16-3135-1{_}6.
23. Hameed, M.S.; Li, Z.; Chen, J.; Qi, J. Lamb-Wave-Based Multistage Damage Detection Method Using an Active PZT Sensor Network for Large Structures. Sensors (Basel, Switzerland) **2019**, 19. https://doi.org/10.3390/s19092010.
24. Zimmermann, E.; Eremin, A.; Lammering, R. Analysis of the continuous mode conversion of Lamb waves in fiber composites by a stochastic material model and laser vibrometer experiments. GAMM-Mitteilungen **2018**, 41. https://doi.org/10.1002/gamm.201800001.
25. Hennings, B.; Lammering, R. Material modeling for the simulation of quasi-continuous mode conversion during Lamb wave propagation in CFRP-layers. Composite Structures **2016**, 151, 142–148. Smart composites and composite structures In honour of the 70th anniversary of Professor Carlos Alberto Mota Soares, https://doi.org/https://doi.org/10.1016/j.compstruct.2016.02.051.
26. Leng, J.; Asundi, A. Structural health monitoring of smart composite materials by using EFPI and FBG sensors. Sensors and Actuators, A: Physical **2003**, 103, 330–340. https://doi.org/10.1016/S0924-4247(02)00429-6.
27. Majumder, M.; Gangopadhyay, T.; Chakraborty, A.; Dasgupta, K.; Bhattacharya, D. Fibre Bragg gratings in structural health monitoring-Present status and applications. Sensors and Actuators, A: Physical **2008**, 147, 150–164. https://doi.org/10.1016/j.sna.2008.04.008.
28. Kinet, D.; Mégret, P.; Goossen, K.W.; Qiu, L.; Heider, D.; Caucheteur, C. Fiber Bragg Grating Sensors toward Structural Health Monitoring in Composite Materials: Challenges and Solutions. Sensors **2014**, 14, 7394–7419. https://doi.org/10.3390/s140407394.
29. Masmoudi, S.; El Mahi, A.; Turki, S. Fatigue behaviour and structural health monitoring by acoustic emission of E-glass/epoxy laminates with piezoelectric implant. Applied Acoustics **2016**, 108, 50–58. Applied Acoustics in Multiphysic systems, https://doi.org/https://doi.org/10.1016/j.apacoust.2015.10.024.
30. Paget, C.A.; Levin, K.; Delebarre, C. Actuation performance of embedded piezoceramic transducer in mechanically loaded composites. Smart Materials and Structures **2002**, 11, 886–891. https://doi.org/10.1088/0964-1726/11/6/309.
31. Qing, X.P.; Beard, S.J.; Kumar, A.; Ooi, T.K.; Chang, F.K. Built-in Sensor Network for Structural Health Monitoring of Composite Structure. Journal of Intelligent Material Systems and Structures **2007**, 18, 39–49. https://doi.org/10.1177/1045389X06064353.
32. Lin, M.; Chang, F.K. The manufacture of composite structures with a built-in network of piezoceramics. Composites Science and Technology **2002**, 62, 919–939. https://doi.org/https://doi.org/10.1016/S0266-3538(02)00007-6.
33. Andreades, C.; Meo, M.; Ciampa, F. Fatigue testing and damage evaluation using smart CFRP composites with embedded PZT transducers. Materials Today: Proceedings **2021**, 34, 260–265. 12th International Conference on Composite Science and Technology, https://doi.org/https://doi.org/10.1016/j.matpr.2020.03.081.
34. Masmoudi, S.; El Mahi, A.; Turki, S. Use of piezoelectric as acoustic emission sensor for in situ monitoring of composite structures. Composites Part B: Engineering **2015**, 80, 307–320. https://doi.org/10.1016/j.compositesb.2015.06.003.
35. Feng, T.; Aliabadi, M.F. Structural Integrity Assessment of Composites Plates with Embedded PZT Transducers for Structural Health Monitoring. Materials **2021**, 14. https://doi.org/10.3390/ma14206148.
36. Andreades, C.; Mahmoodi, P.; Ciampa, F. Characterisation of smart CFRP composites with embedded PZT transducers for nonlinear ultrasonic applications. Composite Structures **2018**, 206, 456–466. https://doi.org/https://doi.org/10.1016/j.compstruct.2018.08.083.
37. Mall, S. Integrity of graphite/epoxy laminate embedded with piezoelectric sensor/actuator under monotonic and fatigue loads*. Smart Materials and Structures **2002**, 11, 527–533. https://doi.org/10.1088/0964-1726/11/4/307.
38. Yang, B.; Xuan, F.Z.; Jin, P.; Hu, C.; Xiao, B.; Li, D.; Xiang, Y.; Lei, H. Damage Localization in Composite Laminates by Building in PZT Wafer Transducers: A Comparative Study with Surface–Bonded PZT Strategy. Advanced Engineering Materials **2018**, 21, 1801040. https://doi.org/10.1002/adem.201801040.
39. Feng, T.; Bekas, D.; Aliabadi, M.H.F. Active Health Monitoring of Thick Composite Structures by Embedded and Surface-Mounted Piezo Diagnostic Layer. Sensors **2020**, 20. https://doi.org/10.3390/s20123410.
40. Su, Z.; Wang, X.; Chen, Z.; Ye, L.; Wang, D. A built-in active sensor network for health monitoring of composite structures. Smart Materials and Structures **2006**, 15, 1939–1949. https://doi.org/10.1088/0964-1726/15/6/050.

41. Giurgiutiu, V.; Zagrai, A.; Bao, J.J. Piezoelectric Wafer Embedded Active Sensors for Aging Aircraft Structural Health Monitoring. SHM Structural Health Monitoring **2002**, pp. 1475–9217. https://doi.org/10.1177/147592170200100104.
42. Kostson, E.; Fromme, P. Fatigue crack growth monitoring in multi-layered structures using guided ultrasonic waves. Journal of Physics: Conference Series **2009**, 195, 012003. https://doi.org/10.1088/1742-6596/195/1/012003.
43. Chan, H.; Masserey, B.; Fromme, P. High frequency guided ultrasonic waves for hidden fatigue crack growth monitoring in multi-layer model aerospace structures. Smart Materials and Structures **2015**, 24, 025037. https://doi.org/10.1088/0964-1726/24/2/025037.
44. Moser, F.; Jacobs, L.J.; Qu, J. Modeling elastic wave propagation in waveguides with the finite element method. NDT & E International **1999**, 32, 225–234. https://doi.org/10.1016/S0963-8695(98)00045-0.
45. Marwitz, S.; Zabel, V. Operational Modal Analysis with a 3D Laser Vibrometer Without External Reference. In Rotating Machinery, Hybrid Test Methods, Vibro-Acoustics & Laser Vibrometry, Volume 8; de Clerck, J.; Epp, D.S., Eds.; Conference Proceedings of the Society for Experimental Mechanics Series, Springer International Publishing: Cham, 2016; pp. 75–85. https://doi.org/10.1007/978-3-319-30084-9{_}7.
46. Debnath, L.; Shah, F.A. Wavelet Transforms and Their Applications; Birkhäuser Boston: Boston, MA, 2015. https://doi.org/10.1007/978-0-8176-8418-1.
47. The MathWorks, I. MATLAB Documentation: Continuous 1-D wavelet transform. Accessed: 2022-01-31.
48. Rauter, N.; Hennings, B.; Neumann, M.N.; Asmus, A.; Lammering, R. Wave Propagation in Elastic Solids: An Analytical Approach. In Lamb-Wave Based Structural Health Monitoring in Polymer Composites; Lammering, R.; Gabbert, U.; Sinapius, M.; Schuster, T.; Wierach, P., Eds.; Research Topics in Aerospace, Springer International Publishing: Cham, 2018; pp. 17–62. https://doi.org/10.1007/978-3-319-49715-0{_}3.